Experimental analysis of gas phase dynamics in a lab scale bubble column operated with deionized water and NaOH solution under uniform bubbly flow conditions

Kipping, R.; Kryk, H.; Hampel, U.;

Originally published:

August 2020

Chemical Engineering Science 229(2021), 116056

DOI: https://doi.org/10.1016/j.ces.2020.116056

Perma-Link to Publication Repository of HZDR:

https://www.hzdr.de/publications/Publ-30434

Experimental analysis of local gas phase hydrodynamics in a lab scale bubble column operated with deionized water and electrolyte solution in mono-dispersed bubbly flow conditions

Ragna Kipping[1], Holger Kryk[2], Uwe Hampel[1,2]

[1] Chair of Imaging Techniques in Energy and Process Engineering,
Technische Universität Dresden, 01062 Dresden, Germany.
[2] Institute of Fluid Dynamics, Helmholtz-Zentrum Dresden - Rossendorf,
Bautzner Landstr. 400, 01328 Dresden, Germany.
*Corresponding author: ragna.kipping@tu-dresden.de

Abstract

We studied the local gas phase hydrodynamics within a lab-scale bubble column operated in the mono-dispersed homogenous bubbly flow regime for two different material systems, namely deionized water and NaOH solution of different concentration. We determined gas holdup distribution, bubble sizes and average axial bubble velocities for up to 18% total gas holdup using ultrafast X-ray computed tomography (UFXCT). Radial gas holdup profiles show wall peaking, which is attributed to the mono-dispersed bubbly flow regime generated by the fine-pore gas sparger used in this study. Experiments with NaOH solution show similar global gas holdup but differ significantly in local gas holdup and bubble size. The Sauter mean diameter was found to decrease with increasing concentration of NaOH, whereby the rate of decrease increases with increasing gas flow rate.

Keywords bubble column hydrodynamics, mono-dispersed bubbly flow, bubble size distribution, bubble rise velocity, electrolyte solutions, Ultrafast X-ray tomography

Nomenclature

Roman symbols

B	retarded van der Waals coefficient	J·m
c_{NaOH}	Concentration of NaOH solution	$mol \cdot l^{-1}$
c_{trans}	Transition concentration for electrolytes	$mol \cdot l^{-1}$
c	Concentration	$mol \cdot l^{-1}$
D	Column diameter	m
$d_{B,eq}$	Equivalent bubble diameter	m
d_S	Sauter mean diameter	m
d_0	Hole diameter of gas sparger	m
f_B	bubble frequency	s^{-1}
H_{col}	Height of the column	m
H_{liq}	Clear liquid height	m
j_G	Superficial gas velocity	$m \cdot s^{-1}$
L	Distance from sparger to measurement height	m
n	Number of bubbles	
r/R	Dimensionless Radis	-
r_B	Radius of the bubble	m
R_g	Gas constant	$J \cdot mol^{-1} \cdot K^{-1}$
t	Time	s
T	Temperature	K
u_{swarm}	Swarm velocity	$m \cdot s^{-1}$
u_z	Average axial gas phase velocity	$m \cdot s^{-1}$
$\dot{V}_{needle}$	Flow rate per needle	$m^3 \cdot s^{-1}$
V_B	Volume of the bubble	m^3
Δz	Axial distance of UFXCT measurement planes	m

Greek symbols

μ	Attenuation coefficient
ε	Gas holdup
σ	Surface tension
ρ	Density
ν	Number of ions

1 Introduction

One of the most commonly used reactor types for gas-liquid reactions in the chemical industry are bubble columns. They are being used when high interfacial area and intense mixing of the liquid phase is important. While their basic design is simple the two-phase flow inside is very complex and hence there are many open questions about the coupling of bubble properties, turbulence, mixing and mass transfer with yield and selectivity of such reactors [1]. Two main types of flow regimes are encountered in bubble column reactors. The homogenous regime exhibits a narrow and uniform bubble size distribution. For air-water systems it occurs at bubble diameters of 2-10 mm if the superficial gas velocity is below j_G = 5 cm·s^{-1} [2]. The breakup and coalescence rates in this regime are low, which results in a uniform bubble size distribution and low back-mixing in the column. At higher gas velocities, the heterogeneous regime can be observed. Here, coalescence and breakup lead to a wider distribution of bubble sizes. Large bubbles appear, which rise with high velocity in the column center while small bubbles accumulate in the wake of large bubbles and in the wall region of the column, where they are entrained due to the liquid back mixing [3]. With regard to the bubble size distribution, the homogenous flow regime can be further subdivided into the mono-dispersed homogenous flow regime and the pseudo-homogenous flow regime [4]. The latter is characterized by a flat or concave shape of radial gas holdup profile and appears predominantly when coarse gas spargers with hole diameters d_0 > 1 mm are used. In the mono-disperse homogenous regime, that is produced by fine spargers with d_0 < 1 mm, gas accumulations near the wall can be found [5–7]. This wall peaking is attributed to the change of sign of lift force for small bubbles (e.g. d_B < 5.8 mm for air-water system [8]), resulting in a net movement of bubbles towards the wall.

Fluid properties have significant influence on the hydrodynamics in gas-liquid systems, especially on the bubble formation, coalescence and break up rates, and thus on the bubble size distribution and gas holdup [9,10]. Gas-liquid systems with electrolyte solutions exhibit an increase of gas holdup compared to air-water systems [11–14]. This is caused by a reduction of coalescence rate while the

break-up rate does not change, which results in a shift of the bubble size distribution towards smaller bubbles [15]. Sujan et al. explained the coalescence inhibition by the increase of the surface elasticity of the gas-liquid interface, which is proportional to the surface tension gradient for single electrolytes and in that way increases the stabilization time of the liquid film [16]. Following the change of bubble size distribution, the homogenous regime is stabilized by the presence of electrolytes and thus the transition from homogenous to heterogeneous regime is shifted towards higher superficial gas velocities [17]. However, a general model for the impact of electrolyte type and concentration does not exist as the involved physical chemistry is complex [13]. Independent of the type of electrolyte a non-linear relation between the gas holdup and electrolyte concentration has been observed. Thus, the impact of the electrolyte is larger at low concentrations, reduces with increasing concentration and eventually vanishes [13,14]. This is encountered by defining a transition concentration c_{trans}, the concentration of an electrolyte above which coalescence suppression is drastically reduced. Therefore, according to Prince and Blanch, a coalescent regime ($c/c_{\mathrm{trans}} \leq 1$) and a non-coalescent regime ($c/c_{\mathrm{trans}} > 1$) can be defined [18] in dependence of the ratio

$$\frac{c}{c_{\mathrm{trans}}} = 1.18\,\nu \left(\frac{B\sigma}{r_{\mathrm{b}}}\right)^{0.5} R_{\mathrm{g}} T \left(\frac{\partial\sigma}{\partial c}\right)^{-2}. \qquad (1)$$

Here, B is the retarded van der Waals coefficient, ν the number of ions formed upon dissociation, r_{b} the radius of the bubble, R_{g} the gas constant, T the temperature, σ the surface tension and $\partial\sigma/\partial c$ the surface tension gradient with concentration [19]. A survey about investigations of the influence of several electrolytes on the bubble column hydrodynamics can be found here [14]. To our knowledge hydrodynamic studies using NaOH solutions are very limited, despite many experimental [20–22] or numerical [23–26] studies on the chemical absorption of carbon dioxide. As an example, Keitel and Onken experimentally determined bubble sizes in NaOH solution and found a decrease of bubble size with increasing ionic strength [15].

The objective of the present study is to investigate the local gas phase hydrodynamics in mono-disperse homogenous bubbly flow for different material systems. For this purpose, experiments with a fine-pore sparger in deionized water and sodium hydroxide solution of different concentrations were

carried out. Radially resolved gas holdup data, bubble size distributions and axial average bubble velocities were measured and analyzed for the different experimental conditions.

2 Materials and methods

2.1 Experimental set up and conditions

Experimental setup

The experimental set up consists of a cylindrical bubble column with 100 mm inner diameter and 2000 mm height. Experiments were carried out using two different designs of a capillary gas distributor. Type A contains a gas chamber and a maximum number of 84 capillaries, having an inner diameter of 0.57 mm each. Type B has a branched structure of tubes for gas feeding and a fixed number of 31 capillaries, each with an inner diameter of 0.22 mm. Both the setup and the gas distributors are schematically depicted in Figure 1a. Experiments were carried out with different fluid properties: I) deionized water and nitrogen and II) NaOH solution of various concentrations and nitrogen. The flow rate of the gas was controlled by a mass flow controller (OMEGA FMA-2609A). The clear liquid height of the column is 1400 mm. All experiments were performed at ambient temperature and pressure conditions.

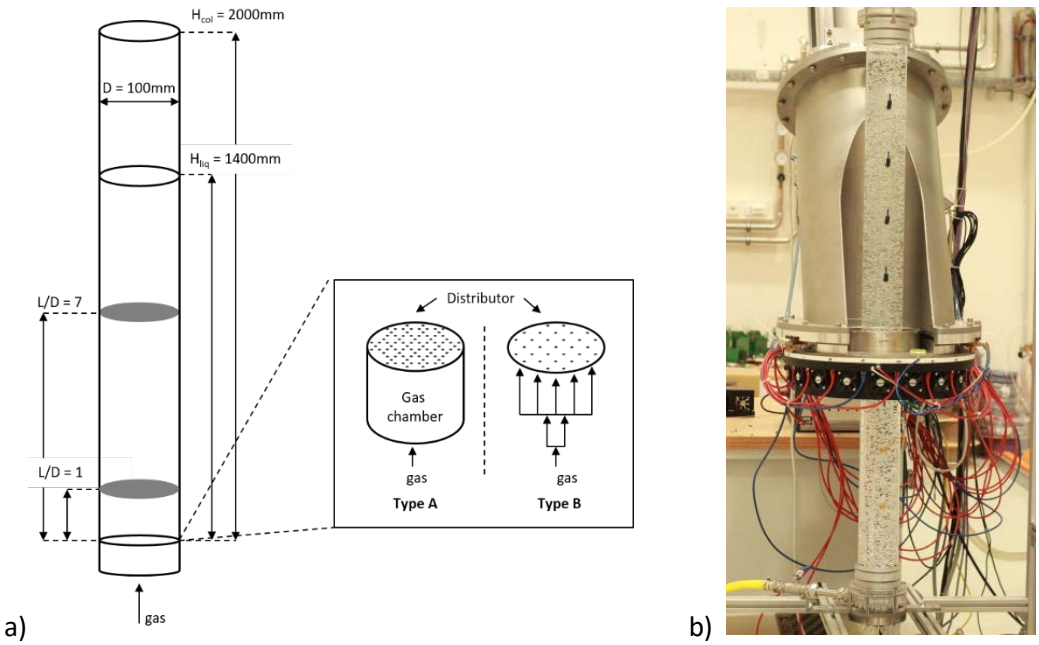

Figure 1: a) Schematic and b) photography of the bubble column in the X-ray scanner.

Measurements were performed at two heights, L/D = 1 and L/D = 7. The superficial velocity of the gas is varied between 0.5 and 2.5 cm·s^{-1} in steps of 0.5 cm·s^{-1} for Type A sparger. For Type B sparger an extended range of superficial gas velocities from 0.2 – 3.5 cm·s^{-1} was examined. For Type B sparger also experiments with sodium hydroxide solution of different concentrations c_{NaOH} = 3.2, 10 and 32 mmol·l^{-1} (corresponding to pH values of 11.5, 12.0 and 12.5) have been conducted. Here, experiments were carried out for superficial gas velocities j_G = 0.5, 1.0, 1.5, 2.0, 2.5, 3.5 cm·s^{-1}. For the intermediate concentration of c_{NaOH} = 10 mmol·l^{-1} a reduced matrix was used, that is, the superficial gas velocity has been increased in steps of 1.0 cm·s^{-1}. Detailed information on the design of the gas spargers can be found in Table 1. For Type A sparger, the number of capillaries was increased with gas flow rate, to achieve similar flow rates for each single needle independent of the overall flow rate and thus generate similar bubble sizes for the entire set of experiments. Contrary, for Type B the number of capillaries was kept constant for all experiments and thus, the flow rate per needle increases linearly with the superficial gas velocity.

Table 1: Overview of the number and arrangement of the needles for the different operating regimes for both sparger types.

Type	A	A	A	A	B
no. of needles	13	19	42	84	31
Position of needles	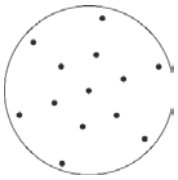	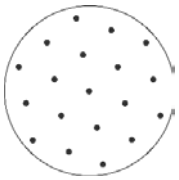	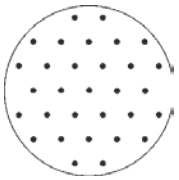	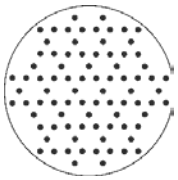	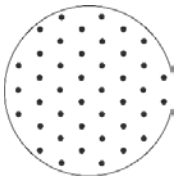
j_G /cm·s^{-1}	0.50	1.0	1.5	2.0 - 2.5	0.2 – 3.5
$\dot{V}_{needle}$ / l·min^{-1}	0.18	0.25	0.17	0.11 - 0.14	0.03 - 0.53

Ultrafast X-ray tomography

Though today there is a variety of measurement techniques available for bubbly flows [27], most of them are intrusive and have limited spatial or temporal resolution. Ultrafast electron beam X-ray computed tomography (UFXCT), that has been developed most recently, is a non-invasive measurement technique that allows multiphase flow imaging with high spatial and temporal resolution [28]. It provides cross-sectional images of the flow, more precisely, of the local fluid density. Hence, it is very well suited for gas-liquid flows. It has been already used for studies on bubble columns with [29] and without internals [29-31], structured packings [33], two-phase flow in pipes [34], solid foams [35] and monoliths [36] but also fluidized beds [37],[38]. The UFXCT scanner is shown in Figure 1b. It consists of a beam gun that generates an electron beam, which is focused on a tungsten target. By electromagnetic deflection of the beam with a high frequency, a moving X-ray source is formed, that is guided along two circular source paths with small axial pitch [39–41]. The radiation is attenuated by the object of interest and recorded by two detector rings. This projection data is then reconstructed using the method of filtered back projection. The experiments presented here were performed with a scanning frequency of 1000 images per second and a spatial resolution of about 1 mm.

Post processing of X-ray image data

The reconstructed data sets are stacks of cross-sectional images of size 180x180 pixels and the X-ray attenuation coefficient $\mu_{\mathrm{i,j,k}}$ as values. Each voxel is described by the spatial coordinates *i* and *j,* and *k* indicates the sampling time. Together with known attenuation coefficients of the empty column μ^{empty} and the full column μ^{full} respectively we calculate the holdup ε as

$$\varepsilon_{\mathrm{i,j,k}} = \frac{\mu_{\mathrm{i,j}}^{\mathrm{full}} - \mu_{\mathrm{i,j,k}}}{\mu_{\mathrm{i,j}}^{\mathrm{full}} - \mu_{\mathrm{i,j}}^{\mathrm{empty}}}. \tag{2}$$

In a next step we need to reconvert the time scale encoded in the index *k* into a length. For that, we need the gas velocity. A simple approach is to compute an average swarm velocity [42]

$$u_{\mathrm{swarm}} = \frac{j_{\mathrm{G}}}{\varepsilon}. \tag{3}$$

However, the drawback of using the empirical swarm velocity is that an average velocity is assigned for each bubble, regardless of its location in the column or local differences of the velocity. Thus, the sizes of fast rising bubbles are underestimated and those of slow rising bubbles are overestimated. To improve the reliability of the data, the average axial gas phase velocity is calculated by applying a cross-correlation function to every pixel of the simultaneously measured gas holdup values of both UFXCT scanning planes. It is important to note, that the evaluation of the velocities was carried out with a plane distance of Δz = 11 mm. The cross-section is divided into ten rings of equal area and the velocity in each ring is determined by spatial averaging. Following the center of each bubble is determined and the corresponding velocity is assigned. Due to this, radial deviations of the global gas phase velocity are considered.

In a third step we apply a binarization and segmentation algorithm (Banowski et al., [43]) that extracts voxel clusters of single bubbles from the data stack. From this, we determine the location and volume V_{B} of each bubble and the bubble equivalent diameter

$$d_{\mathrm{B,eq}} = \sqrt[3]{\frac{6}{\pi} V_{\mathrm{B}}}. \tag{4}$$

Eventually, we determine the average Sauter diameter over all *N* bubbles

$$d_S = \frac{\sum n_i d_{B,eq}^{\ 3}}{\sum n_i d_{B,eq}^{\ 2}}. \quad (5)$$

3 Results and discussion

3.1 Influence of the sparger design

3.1.1 Holdup distribution at $L/D = 1$

In Figure 2 the cross sectional images of the gas holdup distribution for the cross-section at L/D = 1 are depicted for both types of spargers together with the superficial gas velocities. The images proves that the gas feeding of both gas spargers is uniform over the cross-section.

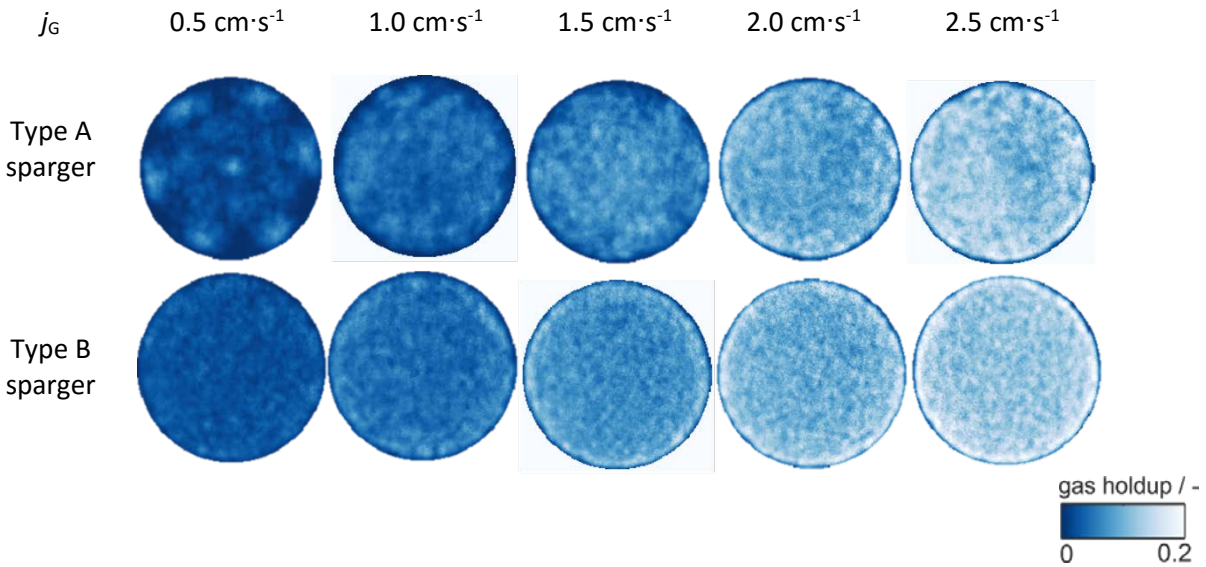

Figure 2: Cross-sectional images of time averaged gas holdup distribution for both sparger types at L/D = 1.

Detailed information about the hydrodynamics are depicted in Figure 3. In Figure 3a the size distribution of the bubbles is shown as volumetric distribution. Thus, for each bubble size class the volume occupied by the respective bubbles is computed and scaled by the total gas volume. Therefore, the area under the curve presents the overall gas holdup. The bubble size distribution at L/D = 1 is considered as the "initial bubble size distribution". Figure 3a shows a comparison of this bubble size distribution for both sparger types. For Type A sparger the average bubble size is d_B = 5-6 mm while it is d_B = 4 - 5 mm for Type B sparger. This results from the smaller inner diameter of the capillaries of

sparger B. For Type B sparger, the bubble size distribution is slightly shifted towards larger bubbles with increasing superficial velocity, since the flow rate per needle increases linearly with the superficial gas velocity. In contrast, for the Type A sparger, the number of needles is increasing with increasing flow rate, giving similar flow rates per needle for the range of superficial gas velocities, resulting in similar bubble sizes for the different cases. Thus, the bubble size distribution is not shifted towards larger bubbles with increasing superficial velocity. For j_G = 2.0-2.5 cm·s^{-1} the peak of the size distribution is similar for both types, although Type A sparger shows a higher portion of larger bubbles. However, both spargers show a narrow distribution, indicating a uniform bubble size and thus homogenous bubbly flow. Figure 3b shows the radial gas holdup profile, which has been determined, corresponding to gas phase velocities for bubble size determination, by dividing the cross section into 10 rings of equal area and then averaging the gas holdup in time in each ring, respectively. The radial gas holdup profile shows a uniform distribution of the gas over the cross section of the column. Wall peaking behavior is observed for Type B sparger, which becomes more significant with increasing flow rate of the gas. Also for Type A sparger this behavior is observed for j_G = 2.0-2.5 cm·s^{-1}.

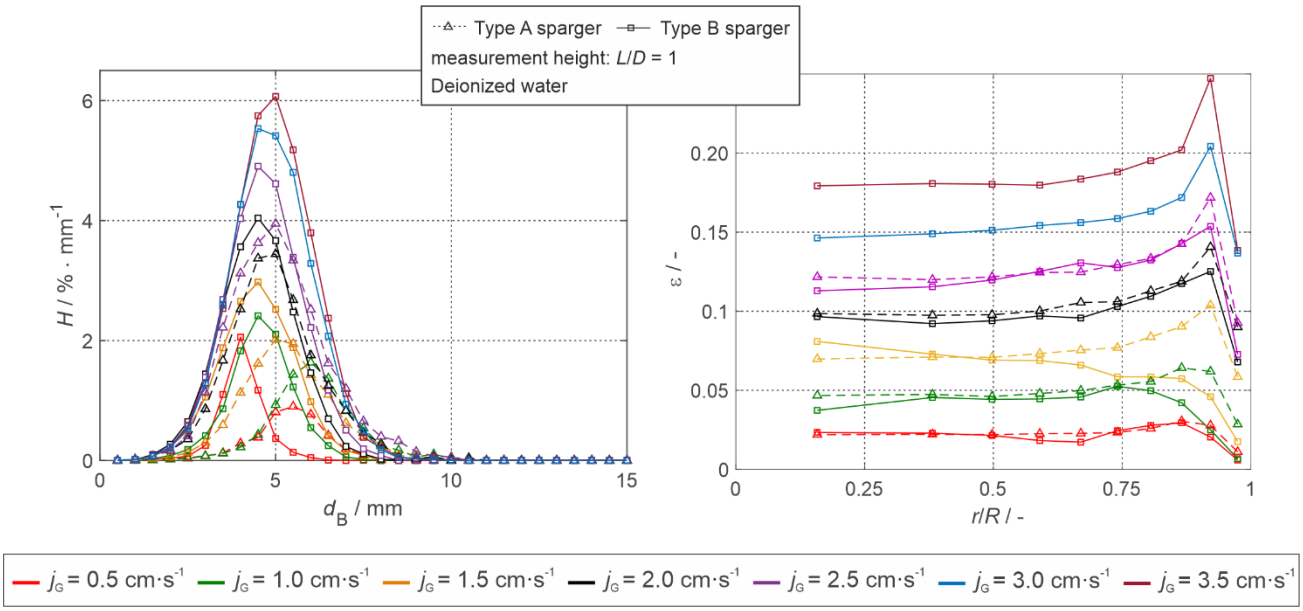

Figure 3: a) Bubble size distribution and b) radial gas holdup profiles at L/D=1 for both sparger types.

3.1.2 Analysis of bubble size distribution and gas holdup in the fully developed bubbly flow region at L/D =7

The following results are for the dimensionless measurement height L/D = 7. Here, the flow is assumed to be fully developed, which is known to be the case for L/D > 5 for this column diameter und operating conditions [3], [44]. Figure 4 shows the overall gas holdup for both sparger types as function of the gas superficial velocity. The global gas holdup is similar for both types of sparger and increases linearly with increasing gas superficial velocity. However, for j_G = 0.5-1.5 cm·s^{-1} the overall gas holdup of sparger A is smaller and contrary for j_G = 2.0-2.5 cm·s^{-1} the overall gas holdup is larger as compared to sparger B. Sparger B produces smaller bubbles at j_G = 0.5-1.5 cm·s^{-1}, having a lower rise velocity and thus leading to an increase in the total gas holdup. For higher superficial gas velocities, the bubble size distributions are similar, which results in similar total gas holdup, too. The time averaged cross-sectional distribution of the gas is depicted as cross-sectional images in Figure 4. From these images a uniform distribution of the time-averaged gas holdup over the cross-section can be concluded, which is a further evidence of homogenous flow and is important for the evaluation of radial gas profiles, where axial symmetry of the flow is assumed.

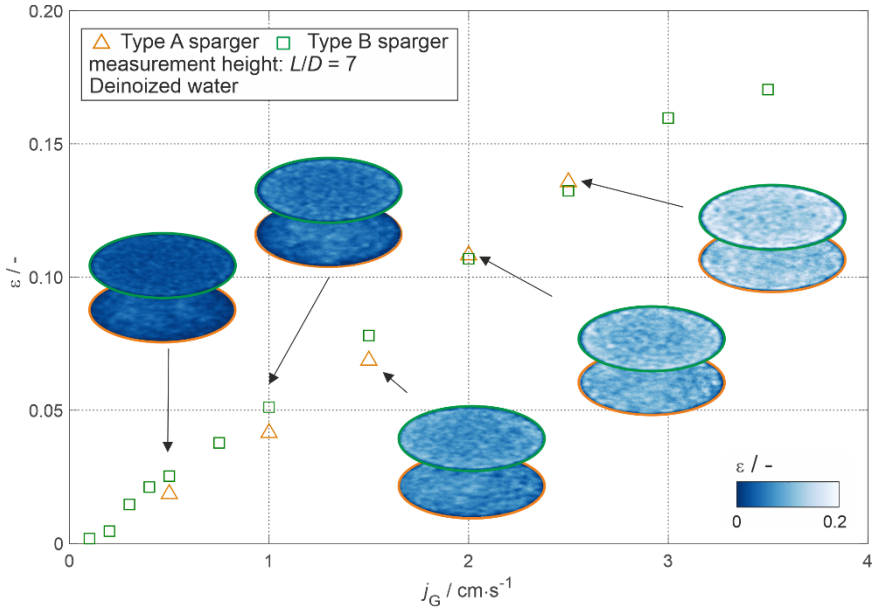

Figure 4: Overall gas holdup as function of superficial gas velocity and images of the time-averaged cross-sectional gas holdup distribution for both sparger types (lower: sparger B, upper: sparger A).

The bubble size distributions for L/D = 7 (Figure 5a) are similar to those at L/D = 1. The radial gas holdup distribution (Figure 5b) indicates differences in the cross-sectional distribution of the gas for both sparger types at similar superficial velocities, which corresponds to the observations at L/D = 1. For j_G = 0.5 - 1.5 cm·s^{-1} the sparger A creates a peak of the gas holdup in the center of the column and while the gas holdup towards the wall region decreases. Contrarily, the gas holdup distribution generated by sparger B shows a uniform distribution of the gas in most of the cross-section and a maximum of the gas holdup at a distance of 5 mm from the wall of the column. However, for all experiments a minimum of the gas holdup can be found at the wall of the column, which is due to a force driving bubbles away from the wall. For j_G = 2.0 - 2.5 cm·s^{-1} the profiles of both spargers are similar and show the behavior, which was described for the sparger B, i.e. a wall peaking behavior. For those cases, also the bubble size distribution is similar, which gives evidence of the strong dependence of bubble size distribution on the radial gas holdup profile. The wall peaking behavior has been also reported by other authors using similar types of gas sparger with hole diameters d_0 < 1mm [5,6,45]. The wall peaking can be explained by the production of smaller bubbles, for which the sign of lift force changes which leads to movement of the bubbles towards the wall region of the column and consequently an increase of gas holdup in this region [8]. For sparger B, with further increase of the superficial gas velocity to j_G = 3.5

cm·s^{-1} the shape of the radial profiles changes and the wall peak disappears. Here larger bubble are produced that tend to migrate to the column center.

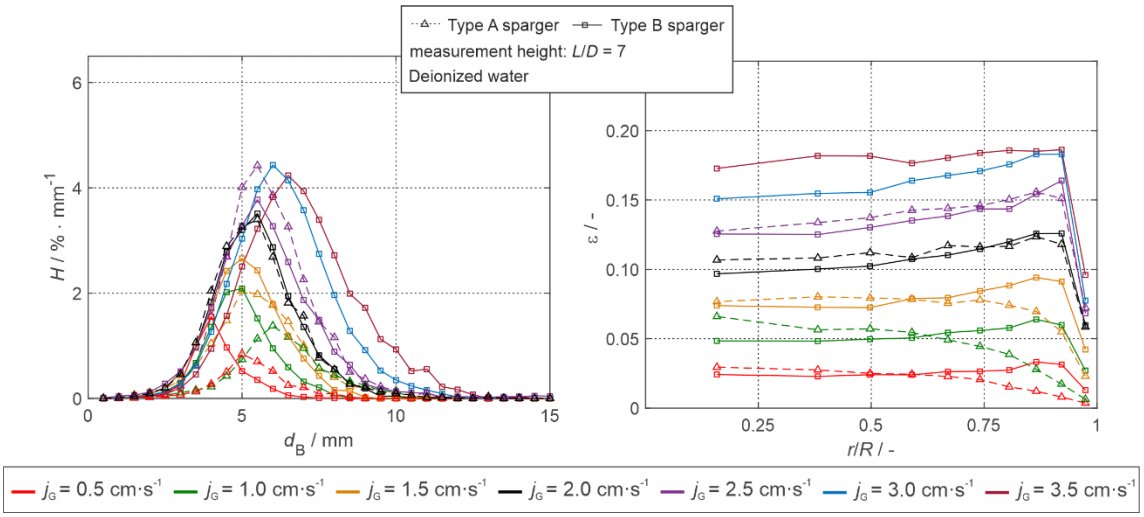

Figure 5: a) Bubble size distribution and b) radial gas holdup distribution for both sparger types at *L*/*D* = 7.

In Figure 6 the Sauter mean diameter is depicted as function of the overall gas holdup for both sparger types, respectively. For sparger A, the Sauter mean diameter is increasing with increasing gas holdup. However, for ε = 0.04 (corresponding to j_G = 1.0 cm·s^{-1}) the Sauter mean diameter is significantly larger, which is in accordance with the higher flow rate of the gas per needle in this case. For sparger B, the Sauter mean diameter is increasing with increasing gas holdup. Furthermore, the increase of the Sauter mean diameter is linear up to a gas holdup of 0.04. Then, the increase of the Sauter mean diameter with gas holdup becomes less, which is in accordance to the findings in the literature [46,47]. The Sauter mean diameter for sparger A is significantly higher in comparison to sparger B. Consequently, also the bubble frequency, which is given in Table 2, is lower in this case.

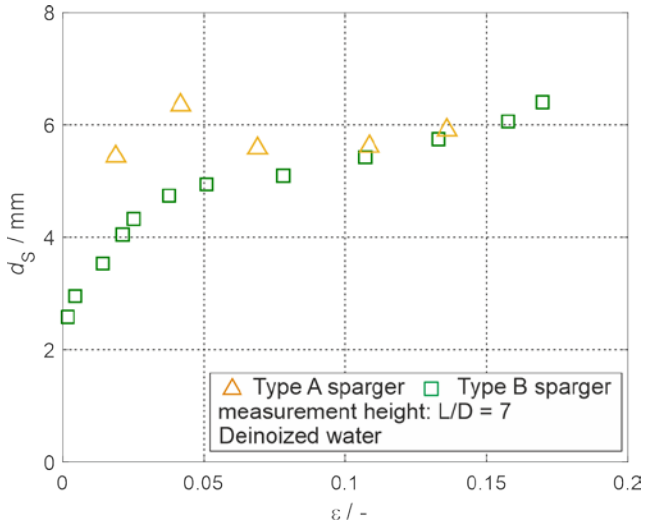

Figure 6: Sauter mean diameter as function of the gas holdup for both sparger types.

The global hydrodynamic data (gas holdup, bubble frequency and Sauter mean diameter) for both sparger types are summarized in Table 2.

Table 2: Global hydrodynamic data (i.e. gas holdup, bubble frequency and Sauter mean diameter) for the two sparger types.

Height	j_G / cm·s^{-1}	ε / -		f_B / s^{-1}		d_S / mm	
		Type A	Type B	Type A	Type B	Type A	Type B
L/D = 1	0.50	0.02	0.03	652.67	843.8	5.40	4.19
	1.00	0.04	0.05	954.67	1136.3	6.04	4.64
	1.50	0.06	0.08	1800	1190.6	5.40	4.45
	2.00	0.10	0.11	2974	2462.7	5.00	4.51
	2.50	0.13	0.13	3155	2561.7	5.23	4.67
L/D = 7	0.50	0.02	0.03	632.2	1465	5.52	4.33
	1.00	0.04	0.05	898.4	1947.6	6.47	4.94
	1.50	0.70	0.08	1467.6	2317.8	5.71	5.11
	2.00	0.11	0.11	1884.6	2808.8	6.24	5.44
	2.50	0.14	0.13	2342.2	2917	6.52	5.68
	3.00	-	0.16	-	3018.4	-	6.06
	3.50	-	0.17	-	3117.2	-	6.41

In Figure 7 the radial profile of the bubble sizes is shown for three different superficial gas velocities and both sparger types in comparison. Contrary to the radial gas holdup profiles, five circular rings with equal diameters are considered. The average bubble size is indicated by square marker. Additionally, the size distribution in each ring is depicted as violin plot according to [48], allowing information about the distribution of small and large bubbles in each ring, respectively. It should be noted, that the bubbles sizes are depicted as number distribution and thus differ from the distributions above.

The radial profile of the bubble size shows a decrease of the mean bubble diameter for sparger A towards the column wall for all superficial velocities. In contrast, the bubble size for sparger B is similar over the whole cross section. Additionally, the overall bubble sizes for sparger A in each circular ring are higher in comparison to sparger B, except close to the wall. Detailed information and derivations about the flow structure can be obtained from the size distributions in each ring, respectively. For j_G = 0.5 cm·s^{-1} the violin plots show similar shapes for both types of sparger in the center of the column. However, the shape of the distribution in the wall region is significantly different and indicates an attraction of smaller bubbles in the wall region of the column for sparger A, which is not the case for sparger B. A similar behavior can be obtained for sparger A and j_G = 1.5 cm·s^{-1}. However, already at r/R = 0.7 the number of smaller bubbles is increasing. Whereas the distribution is shifted towards larger bubbles in the center, it turns towards smaller bubbles in the wall region for this sparger type. Contrary the distributions for sparger B are similar over the complete cross-section with slight increase of the proportion of smaller bubbles in the wall region. Also, for j_G = 2.5 cm·s^{-1} a shift of the bubble size distribution towards smaller bubbles can be obtained for both sparger types, although this is not as pronounced as for the other superficial velocities and thus there is a less decrease of the overall bubble size.

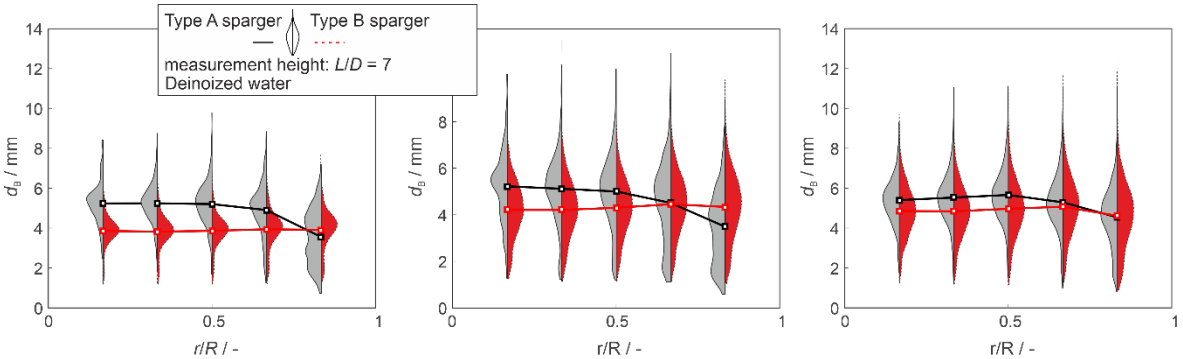

j_G = 0.5 cm·s^{-1} j_G = 1.5 cm·s^{-1} j_G = 2.5 cm·s^{-1}

Figure 7: Radial profile of bubble sizes and corresponding violin plot of the bubble size distribution for both sparger types (red: Type A sparger, black: Type B sparger). Violin plot according to [48].

3.2 Influence of sodium hydroxide concentration

For sparger B additional experiments with sodium hydroxide solution have been performed. For electrolyte solutions the gas holdup is known to increase with increasing electrolyte concentration. However, this effect vanishes at a transition concentration, which is unique for each electrolyte. For NaOH solution a value of c_{trans} = 0.084 mol·l^{-1} was experimentally determined by Zahradnik et al. [49]. Thus, the ratios of c/c_t in our investigations are c/c_t = 0.04, 0.12 and 0.38. In Table 3 the overall gas holdup and bubble frequencies obtained from UFXCT images are summarized for experiments using NaOH solution and all superficial gas velocities. Contrary to the observations in literature, the gas holdup is similar with increasing concentration of sodium hydroxide solution and comparable to the measurements using deionized water. From literature a linear dependence of the gas holdup with increasing electrolyte concentrations is known, which is explained by the coalescence suppression for $c/c_t < 1$. Generally, coalescence phenomena are known to be less in homogenous flow regime, where our experiments have been conducted and thus this effect in our investigations is not as pronounced as in other studies. However, differences can be obtained for the bubble frequencies, which are increasing with increasing concentration of sodium hydroxide solution at equal gas flow rates.

Table 3: Overall gas holdup and bubble frequencies for the different concentrations of NaOH solution and superficial velocities.

j_G / cm·s^{-1}	ε / -			f_B / s^{-1}		
	c/c_t = 0.04	c/c_t = 0.12	c/c_t = 0.38	c/c_t = 0.04	c/c_t = 0.12	c/c_t = 0.38
0.50	0.02	0.02	0.02	1417.8	1445.7	1558.1
1.00	0.04	-	0.04	1703.6	-	1920.9
1.50	0.07	0.07	0.07	2416.2	2593.7	3278.3
2.00	0.09	-	0.10	2979.2	-	4861.0
2.50	0.12	0.12	0.13	3113.6	3472.9	5362.7
3.50	0.17	0.17	0.17	3252.6	3593.7	5491.1

Consequently, the Sauter mean diameter is decreasing with increasing concentration of NaOH solution (Figure 8), which is in accordance with literature. However, the slope of decrease is a seen to be a function of the superficial gas velocity. In particular, with increasing superficial gas velocity, a stronger decrease of the Sauter mean diameter can be obtained.

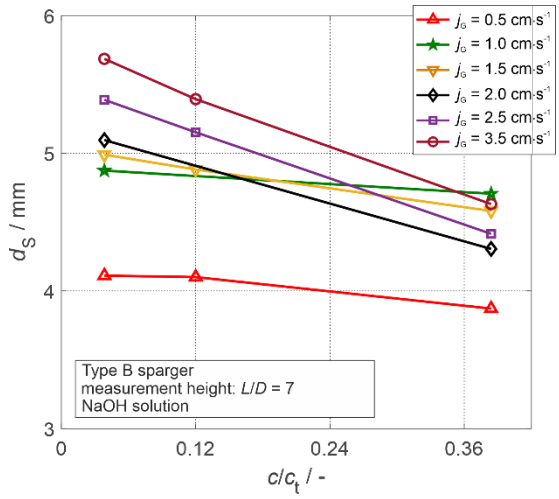

Figure 8: Sauter mean diameter as function of ratios of c/c_t for different superficial gas velocities.

The comparison of local gas holdup data for the different fluids is depicted in Figure 9 for a superficial gas velocity of j_G = 3.5 cm·s^{-1}. This case is considered as representative, because the influence of the change of the fluid is most pronounced for this case. Figure 9a shows the radial gas holdup profile. The radial profile for deionized water is flat. In contrast, NaOH solution shows a peak of the gas holdup in the wall region, which becomes higher with increasing concentration of NaOH solution. The reason for this lies in the formation of smaller bubbles and similar to the cases of low superficial gas velocity for deionized water the lift force, driving bubbles towards the column wall. In Figure 9b the radial profile of the bubble size distribution is depicted for j_G = 3.5 cm·s^{-1} and deionized water and sodium hydroxide solution with c/c_t =0.38. Besides the differences of the overall bubble size, discussed above, the distribution of small and large bubbles is different. For deionized water a large amount of small bubbles accumulate in the wall region, leading to a clear decrease of the overall bubble size in this area. Contrary, for sodium hydroxide solution the bubble size remains the same over the whole cross-section and thus a more homogenous flow structure.

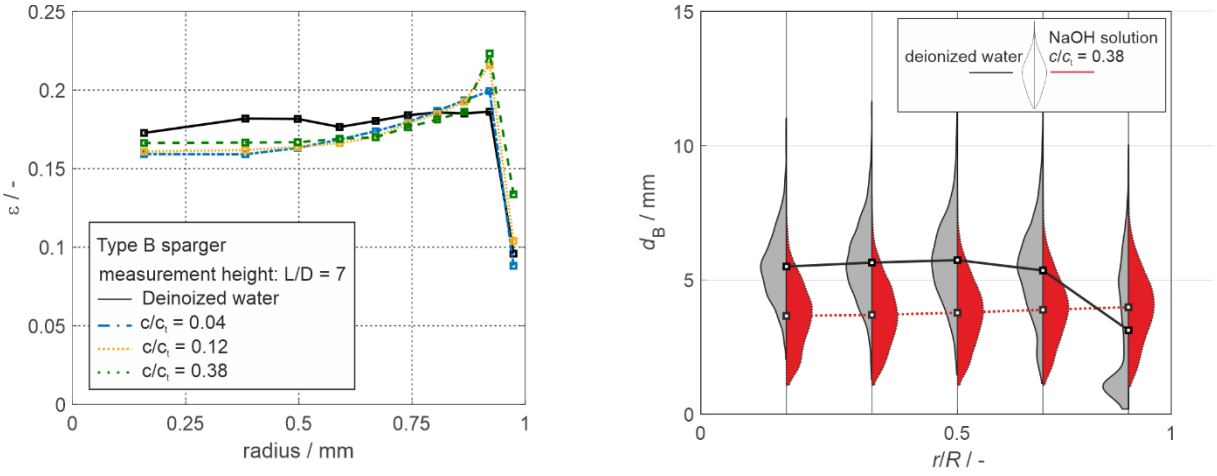

Figure 9: Comparison of a) radial gas holdup profile and b) radial bubble size distribution for deionized water and sodium hydroxide solution for j_G = 3.5 cm·s^{-1}.

3.3 Average gas phase velocities

In Figure 10 the average gas phase velocities are depicted in dependence of the gas superficial velocity for both sparger types and the different concentrations of sodium hydroxide solutions for Type B sparger, respectively. It is worth mentioning, that the average axial velocity in the upward direction u_z is considered. The overall axial bubble velocity u_z is seen to decrease slowly with increasing superficial gas velocity due to the collective effect of bubbles [47][13]. The so called hindrance effect is explained by the interactions of the bubble wakes, which lead to an attenuation of the single bubble wakes and in turn a reduction of the rise velocity of the bubbles [50]. For Type B sparger and gas holdup of ε ≈ 0.02 the average gas phase velocity is about u_z = 29 cm·s^{-1} regardless of the fluid. In contrast for Type A sparger the corresponding data point shows an axial gas phase velocity of u_z = 25 cm·s^{-1}. With increasing gas holdup the average gas phase velocity for Type B sparger and deionized water is decreasing for 0.02 < ε < 0.13. For ε ≥ 0.13 (corresponds to j_G ≥ 2.5 cm·s^{-1}) an increase of the axial velocity is observed, while the bubble size is not increasing significantly (see bubble size distribution in Figure 5). Contrary, for the cases of NaOH solution the decrease of the rise velocity also continues for ε ≥ 0.13, which is in agreement with stabilization of the homogenous flow regime by electrolyte solutions. In principle, the average axial velocities of NaOH solution are higher compared to deionized water. In Figure 10 also a comparison to experimental data from Colombet et al. is provided [47]. Their results, which represent the vertical bubble velocity in the column center, were obtained by different

optical measurement techniques (e.g. dual-tip optical probe and Particle Tracking Velocimetry) for rectangular bubble column with bubbles $d_B \leq 4$ mm diameter and $\varepsilon \leq 0.20$. The course of the decrease is similar to our measurement data. However, lower values of the velocities have been obtained, which result from the smaller bubble sizes in their study.

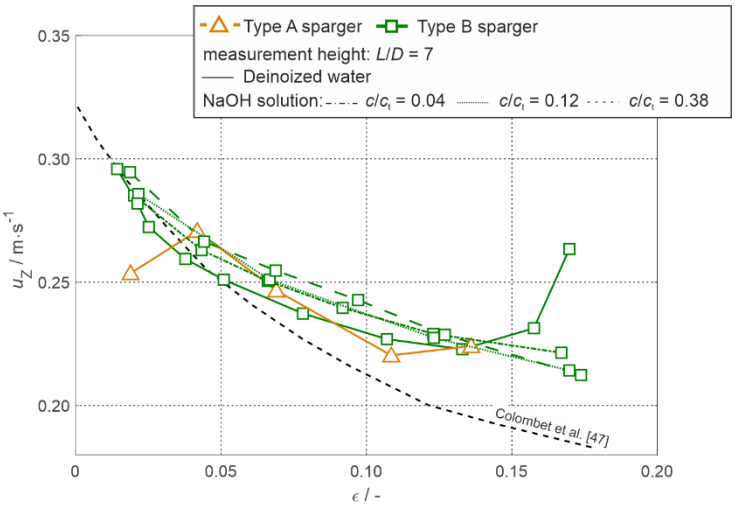

Figure 10: Average gas phase velocity in upward flow direction for both sparger types and different concentrations of sodium hydroxide solution without considering the wall region.

In Figure 11 the radial distribution of the axial bubble velocity is depicted. According to the analysis of the radial gas holdup the cross-section is divided in 10 rings of equal area, in which the average gas phase velocity is determined. From the comparison of the radial distribution of the axial gas phase velocity of the two sparger Types in Figure 11a, information about the flow structures can be derived. Type A sparger exhibits a gradient of the velocity from the center to the wall region, which is in accordance to the radial gas holdup profile as well as the larger bubble diameter produced by this sparger. In contrast, the Type B sparger shows a uniform distribution of the axial gas phase velocity, which is a further evidence for the homogenous flow structure in the bubble column. However, with increasing flow rate, the shape of the radial profile also for this type of sparger is changing. For $j_G = 3.5$ cm·s^{-1} the velocity profile obtains a parabolic shape similar to those of Type A sparger. The reason for this lies in the further increased bubble size and thus a change of the flow structure. The attraction of the bubbles to the wall region becomes less. In turn, a higher portion of bubbles is located in the center of the column, which leads to large increase of the axial gas phase velocity in this region and in the

whole cross-section. In Figure 11b, the radial profile of the axial gas phase velocity is shown for deionized water and sodium hydroxide solution. Here, for reasons of clarity, only the results for the superficial velocity $j_G = 3.5$ cm·s^{-1} are depicted. As mentioned before a parabolic velocity profile has be obtained for the case of deionized water. Contrary, using sodium hydroxide solution the profile alters to a uniform flat shape and a significant reduction of the axial velocity in the center of the column, which is due to the smaller bubbles formed for the electrolyte solution. Furthermore, the profile is seen to become more uniform with increasing concentration of sodium hydroxide solution.

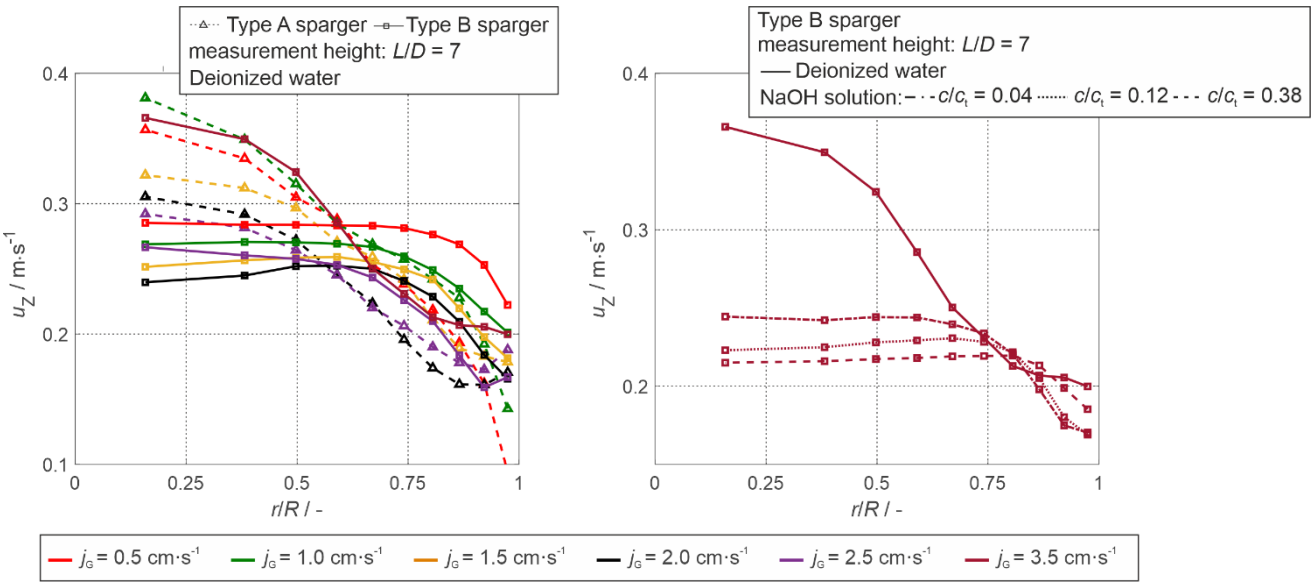

Figure 11: Radial profiles of axial gas velocity a) comparison of sparger design for deionized water and b) comparison of different NaOH concentration for $j_G = 3.5$ cm·s^{-1}.

4 Summary and conclusion

A comprehensive study on the influence of sparger Type (number of needles and opening diameter) and fluid properties (deionized water and sodium hydroxide solution) on the local gas phase hydrodynamics has been performed. Applying UFXCT, detailed information about bubble sizes and gas holdup distribution as well as axial gas bubble velocities were gained. The main findings of this study summarized as follows:

- Wall peaking behavior has been observed for the radial gas holdup profiles for most of the cases, which is in accordance with other studies that employed similar spargers, i.e. fine pore

spargers with small hole diameter (d_0 < 1 mm). The effect can be explained by the change of sign of the lift force for small bubbles, and thus an accumulation of the gas in the wall region.

- The overall gas holdup for water and NaOH solution is similar, which is in contrast to previous findings in the literature of increasing gas holdup with electrolyte concentration. However, the bubble frequency is found to increase and consequently the Sauter mean diameter is found to decrease with the use of NaOH solution and increasing concentration.
- The Sauter mean diameter is linearly decreasing with increasing concentration of NaOH solution. Furthermore it was found, that the slope of decrease is increasing with increasing flow rate of the gas. To our knowledge, this effect is not reported in the literature so far due to lack of experimental data.
- The average gas phase velocity is found to decrease with increasing gas hold up up to a critical gas holdup of ε = 0.13 (i.e. superficial gas velocity) for deionized water due to the hindrance effect of the bubbles. For electrolyte solution, this critical value does not exist in the investigated range of gas holdup and may be shifted towards higher gas flow rates. Thus, the use of electrolyte solution leads to a stabilization of the homogenous flow regime.

5 References

[1] N. Kantarci, Bubble column reactors, Process Biochem. 40 (2005) 2263–2283. http://www.sciencedirect.com/science/article/pii/S0032959204004418%5Cnhttp://doi.wiley.com/10.1002/jctb.280580416.

[2] A. Shaikh, M.H.M. Al-Dahhan, A review on flow regime transition in bubble columns, Int. J. Chem. React. Eng. 5 (2007).

[3] P. Gupta, B. Ong, M.H. Al-dahhan, M.P. Dudukovic, B.A. Toseland, Hydrodynamics of churn turbulent bubble columns : gas – liquid recirculation and mechanistic modeling, Catal. Today. 64 (2001) 253–269.

[4] G. Besagni, F. Inzoli, T. Ziegenhein, Two-Phase Bubble Columns: A Comprehensive Review, ChemEngineering. 2 (2018) 13.

[5] S. Sharaf, M. Zednikova, M.C. Ruzicka, B.J. Azzopardi, Global and local hydrodynamics of bubble columns - Effect of gas distributor, Chem. Eng. J. 288 (2016) 489–504.

[6] R. Mudde, Uniform flow in bubble columns, Ind. Eng. Chem. Res. 48 (2009) 148–158.

[7] M.C. Ruzicka, J. Drahoš, P.C. Mena, J.A. Teixeira, Effect of viscosity on homogeneous-heterogeneous flow regime transition in bubble columns, in: Chem. Eng. J., 2003: pp. 15–22.

[8] A. Tomiyama, H. Tamai, I. Zun, S. Hosokawa, Transverse migration of single bubbles in simple shear flows, Chem. Eng. Sci. 57 (2002) 1849–1858.

[9] G. Besagni, F. Inzoli, The effect of liquid phase properties on bubble column fluid dynamics: Gas holdup, flow regime transition, bubble size distributions and shapes, interfacial areas and foaming phenomena, Chem. Eng. Sci. 170 (2017) 270–296.

[10] P. Rollbusch, M. Becker, M. Ludwig, A. Bieberle, M. Grünewald, U. Hampel, R. Franke, Experimental investigation of the influence of column scale , gas density and liquid properties on gas holdup in bubble columns, Int. J. Multiph. FLOW. 75 (2015) 88–106. https://doi.org/10.1016/j.ijmultiphaseflow.2015.05.009.

[11] C.P. Ribeiro, D. Mewes, The influence of electrolytes on gas hold-up and regime transition in bubble columns, Chem. Eng. Sci. 62 (2007) 4501–4509. https://doi.org/10.1016/j.ces.2007.05.032.

[12] H. Hikita, S. Asai, K. Tanigawa, K. Segawa, M. Kitao, Gas hold-up in bubble columns, Chem. Eng. J. 20 (1980) 59–67. https://doi.org/10.1016/0300-9467(80)85006-4.

[13] H. Kellermann, K. Jüttner, G. Kreysa, Dynamic modelling of gas hold-up in different electrolyte systems, J. Appl. Electrochem. 28 (1998) 311–319. https://doi.org/10.1023/A:1003219917662.

[14] G. Besagni, F. Inzoli, Influence of electrolyte concentration on holdup, flow regime transition and local flow properties in a large scale bubble column, J. Phys. Conf. Ser. 655 (2015). https://doi.org/10.1088/1742-6596/655/1/012039.

[15] G. Keitel, U. Onken, 1982_Keitel.pdf, Chem. Eng. Sci. 37 (1982) 1635–1638. https://doi.org/10.1016/0009-2509(82)80033-X.

[16] A. Sujan, R.K. Vyas, Estimation of transition concentration of aqueous mixtures of single and binary electrolytes for bubble coalescence inhibition, Chem. Pap. 72 (2018) 2539–2559. https://doi.org/10.1007/s11696-018-0470-2.

[17] S. Orvalho, M.C. Ruzicka, J. Drahos, Bubble column with electrolytes: Gas holdup and flow regimes, Ind. Eng. Chem. Res. 48 (2009) 8237–8243. https://doi.org/10.1021/ie900263d.

[18] R.R. Lessard, S.A. Zieminski, Bubble Coalescence and Gas Transfer in Aqueous Electrolytic Solutions, Ind. Eng. Chem. Fundam. 10 (1971) 260–269. https://doi.org/10.1021/i160038a012.

[19] M.J. Prince, H.W. Blanch, Transition electrolyte concentrations for bubble coalescence, AIChE J. 36 (1990) 1425–1429. https://doi.org/10.1002/aic.690360915.

[20] D. Darmana, R.L.B. Henket, N.G. Deen, J.A.M. Kuipers, Detailed modelling of hydrodynamics, mass transfer and chemical reactions in a bubble column using a discrete bubble model: Chemisorption of CO2 into NaOH solution, numerical and experimental study, Chem. Eng. Sci. 62 (2007) 2556–2575. https://doi.org/10.1016/j.ces.2007.01.065.

[21] C. Fleischer, S. Becker, G. Eigenberger, Detailed modeling of the chemisorption of CO2 into NaOH in a bubble column, Chem. Eng. Sci. 51 (1996) 1715–1724. https://doi.org/10.1016/0009-2509(96)00030-9.

[22] R. Kipping, H. Kryk, E. Schleicher, M. Gustke, U. Hampel, Application of a Wire-Mesh Sensor for the Study of Chemical Species Conversion in a Bubble Column, Chem. Eng. Technol. 40 (2017) 1425–1433. https://doi.org/10.1002/ceat.201700005.

[23] M. Krauβ, R. Rzehak, Reactive absorption of CO2in NaOH: Detailed study of enhancement factor models, Chem. Eng. Sci. 166 (2017) 193–209.

https://doi.org/10.1016/j.ces.2017.03.029.

[24] M. Krauß, R. Rzehak, Reactive absorption of CO2 in NaOH: An Euler-Euler simulation study, Chem. Eng. Sci. 181 (2018) 199–214. https://doi.org/10.1016/j.ces.2018.01.009.

[25] Hlawitschka, Drefenstedt, Bart, Local Analysis of CO 2 Chemisorption in a Rectangular Bubble Column Using a muliphase Euler-Euler CFD code, J. Chem. Eng. Process Technol. 7 (2016).

[26] M.C. Gruber, S. Radl, J.G. Khinast, Rigorous modeling of CO2 absorption and chemisorption: The influence of bubble coalescence and breakage, Chem. Eng. Sci. 137 (2015) 188–204. https://doi.org/10.1016/j.ces.2015.06.008.

[27] C. Boyer, A.-M. Duquenne, G. Wild, Measuring techniques in gas–liquid and gas–liquid–solid reactors, Chem. Eng. Sci. 57 (2002) 3185–3215. http://www.sciencedirect.com/science/article/pii/S0009250902001938.

[28] F. Fischer, U. Hampel, Ultra fast electron beam X-ray computed tomography for two-phase flow measurement , Nucl. Eng. Des. . 240 (2010) 2254–2259. http://www.sciencedirect.com/science/article/pii/S0029549309005755.

[29] F. Möller, Y.M. Lau, T. Seiler, U. Hampel, M. Schubert, A study on the influence of the tube layout on sub-channel hydrodynamics in a bubble column with internals, Chem. Eng. Sci. 179 (2018) 265–283. https://doi.org/10.1016/j.ces.2018.01.008.

[30] S. Rabha, M. Schubert, M. Wagner, D. Lucas, U. Hampel, Bubble size and radial gas hold-up distributions in a slurry bubble column using ultrafast electron beam X-ray tomography, AIChE J. 59 (2013) 1709–1722.

[31] S. Azizi, A. Yadav, Y.M. Lau, U. Hampel, S. Roy, M. Schubert, On the experimental investigation of gas-liquid flow in bubble columns using ultrafast X-ray tomography and radioactive particle tracking, Chem. Eng. Sci. 170 (2017) 320–331. https://doi.org/10.1016/j.ces.2017.02.015.

[32] Y.M. Lau, K. Muller, S. Azizi, M. Schubert, Voronoi analysis of bubbly flows via ultrafast X-ray tomographic imaging, Exp. Fluids. 57 (2016) 1–12. https://doi.org/ARTN 35\r10.1007/s00348-016-2118-8.

[33] J. Sohr, M. Schubert, S. Flechsig, E.Y. Kenig, U. Hampel, Experimental Investigation of the Froth Height in Columns with Sandwich Packings, Chemie-Ingenieur-Technik. 91 (2019) 139–144. https://doi.org/10.1002/cite.201800069.

[34] M. Banowski, M. Beyer, L. Szalinski, D. Lucas, U. Hampel, Comparative study of ultrafast X-ray tomography and wire-mesh sensors for vertical gas–liquid pipe flows, Flow Meas. Instrum. 53 (2017) 95–106. https://doi.org/10.1016/j.flowmeasinst.2016.02.001.

[35] J. Zalucky, M. Wagner, M. Schubert, R. Lange, U. Hampel, Hydrodynamics of descending gas-liquid flows in solid foams: Liquid holdup, multiphase pressure drop and radial dispersion, Chem. Eng. Sci. 168 (2017) 480–494. https://doi.org/10.1016/j.ces.2017.05.011.

[36] T. Schäfer, C. Meitzner, R. Lange, U. Hampel, A study of two-phase flow in monoliths using ultrafast single-slice X-ray computed tomography, Int. J. Multiph. Flow. 86 (2016) 56–66. https://doi.org/10.1016/j.ijmultiphaseflow.2016.07.008.

[37] V. Verma, J.T. Padding, N.G. Deen, J.A.M. Hans Kuipers, F. Barthel, M. Bieberle, M. Wagner, U. Hampel, Bubble dynamics in a 3-D gas-solid fluidized bed using ultrafast electron beam X-ray tomography and two-fluid model, AIChE J. 60 (2014) 1632–1644. https://doi.org/10.1002/aic.14393.

[38] M. Bieberle, F. Barthel, U. Hampel, Ultrafast X-ray computed tomography for the analysis of gas-solid fluidized beds, Chem. Eng. J. 189–190 (2012) 356–363. https://doi.org/10.1016/j.cej.2012.02.028.

[39] M. Bieberle, F. Barthel, Ultrafast electron beam X-ray computed tomography for 2D and 3D

two-phase flow imaging, Imaging Syst. …. (2012). http://ieeexplore.ieee.org/xpls/abs_all.jsp?arnumber=6295548 (accessed September 25, 2014).

[40] M. Bieberle, F. Barthel, H.-J. Menz, H.-G. Mayer, U. Hampel, Ultrafast three-dimensional x-ray computed tomography, Appl. Phys. Lett. 98 (2011). http://scitation.aip.org/content/aip/journal/apl/98/3/10.1063/1.3534806.

[41] M. Neumann, M. Bieberle, M. Wagner, A. Bieberle, U. Hampel, Improved axial plane distance and velocity determination for ultrafast electron beam x-ray computed tomography, Meas. Sci. Technol. 30 (2019). https://doi.org/10.1088/1361-6501/ab1ba2.

[42] W.D. Deckwer, R.W. Field, Bubble column reactors, Wiley, 1992. http://books.google.de/books?id=0aQQAQAAMAAJ.

[43] M. Banowski, D. Lucas, L. Szalinski, A new algorithm for segmentation of ultrafast X-ray tomographed gas-liquid flows, Int. J. Therm. Sci. 90 (2015) 311–322. https://doi.org/10.1016/j.nucengdes.2009.11.016.

[44] X. Luo, D. Lee, R. Lau, G. Yang, L. Fan, Maximum stable bubble size and gas holdup in high-pressure slurry bubble columns, AIChE J. 45 (1999) 665–680. http://onlinelibrary.wiley.com/doi/10.1002/aic.690450402/abstract (accessed September 25, 2014).

[45] W. Harteveld, Bubble columns, Technische Universiteit Delft, 2005.

[46] M. Simonnet, C. Gentric, E. Olmos, N. Midoux, Experimental determination of the drag coefficient in a swarm of bubbles, Chem. Eng. Sci. 62 (2007) 858–866. https://doi.org/10.1016/j.ces.2006.10.012.

[47] D. Colombet, D. Legendre, F. Risso, A. Cockx, P. Guiraud, Dynamics and mass transfer of rising bubbles in a homogenous swarm at large gas volume fraction, J. Fluid Mech. 763 (2014) 254–285. https://doi.org/10.1017/jfm.2014.672.

[48] L. Hintze, R.D. Nelson, Violin Plots: A Box Plot-Density Trace Synergism, Am. Stat. 52 (2010) 181–184.

[49] J. Zahradník, M. Fialová, V. Linek, The effect of surface-active additives on bubble coalescence in aqueous media, Chem. Eng. Sci. 54 (1999) 4757–4766. https://doi.org/10.1016/S0009-2509(99)00192-X.

[50] F. Risso, V. Roig, Z. Amoura, G. Riboux, A.-M. Billet, Wake attenuation in large Reynolds number dispersed two-phase flows., Philos. Trans. A. Math. Phys. Eng. Sci. 366 (2008) 2177–90. https://doi.org/10.1098/rsta.2008.0002.

6 Acknowledgement

This work was supported by the German Research Foundation (DFG), reactive bubbly flows

(SPP1740; HA3088/8-1, HA3088/8-2).